Case Studies in Chemical and Environmental Engineering 7 (2023) 100301

Contents lists available at ScienceDirect

Case Studies in Chemical and Environmental Engineering

journal homepage: www.sciencedirect.com/journal/case-studies-in-chemical-and-environmental-engineering

Case Report

Enhancing photodegradation of methylene blue and reusability using CoO/ZnO composite nanoparticles

Nugraheni Puspita Rini, Nurul Imani Istiqomah, Sunarta, Edi Suharyadi *

Department of Physics, Universitas Gadjah Mada, Yogyakarta, Indonesia

ARTICLE INFO

Keywords:
Composite
CoO
Nanoparticles
Methylene blue
Photocatalyst
ZnO

ABSTRACT

This study investigates photocatalytic activity performance of CoO/ZnO nanoparticles (NPs). CoO NPs was synthesized under the hydrothermal method, followed by calcination, while CoO/ZnO NPs were successfully synthesized using the precipitation method with various molar ratios of ZnO. X-ray diffraction and selected area electron diffraction showed that CoO and ZnO have a hexagonal structure; another phase appeared as a Co_3O_4 spinel cubic structure. The crystallite size was decreased as the ZnO concentration increased. The transmission electron microscopy image of CoO/ZnO showed almost spherical, non-uniform, and slightly dispersed under agglomerated conditions with the particle size of 17.4 ± 3.5 and 18.1 ± 4.1 nm for molar ratio of 1:2 and 1:3, respectively. Besides, the corresponding chemical elements are confirmed by energy-dispersive X-ray spectroscopy. Fourier-transform infrared spectra showed metallic functional groups, such as C_{tet}^{2+}-O, C_{oct}^{3+}-O, and Zn–O at 586.36, 671.23, and 410–429 cm^{-1} also suggests the formation of NPs. A vibrating sample magnetometer showed that the CoO/ZnO NPs exhibited antiferromagnetic properties. However, redshift absorption and band gap narrowing were observed only with the ZnO addition. The removal efficiency of photodegradation methylene blue was optimal for CoO/ZnO at a concentration of 1:2, reached 67.5% degradation within 3 h for uptake every 30 min. The photodegradation was also analyzed using a Langmuir-Hinshelwood kinetic model, resulting a rate constant (K_{app}) of 6.428 × 10^{-3} min^{-1} and a half-life time ($t_{1/2}$) of 107.84 ± 0.01 min at the optimum concentration. The NPs could be reused up to three times without significant change of activity. Therefore, CoO/ZnO NPs is promising photocatalyst to be developed in removal of organic pollutants in various environments.

1. Introduction

Water contamination due to the extensive use of dyes in the printing and dyeing, textile, cosmetics, and leather sectors has progressively led to serious environmental issues [1]. Dyes are aromatic molecular structure that is difficult to be degraded. They are anticipated to be strong and stable against oxidizing agents, thus making them more resistant to biodegradation, resulting in high concentrations of dyes in the environment. According to earlier studies, people who are exposed to contaminated water for an extended period, even at extremely low quantities, are at risk for suffering various ailments, such as cyanosis, tissue necrosis, Heinz body formation, jaundice, increased heartbeat rate, and cancer [2]. The presence of dyes can also produce vivid colour, which can affect transparency and water gas solubility, thus adversely affecting aquatic biota by reducing sunlight transmission and limiting photosynthesis, which causing oxygen deficiency [3]. Therefore, developing efficient and effective techniques to remove dye waste is crucial for maintaining ecological balance and safeguarding human health. Many technologies have been used in dealing with dye waste, including adsorption, chemical coagulation, biodegradation, and electrolysis [4,5]. However, increased energy costs and secondary pollutants have compelled researchers to look for more effective and sustainable water treatment systems. Even though many physical and chemical approaches have been developed to remove dyes and other organic substances, they may encounter challenges, such as producing secondary pollution and extra energy cost [6]. Distantly, photocatalytic technology has gained recognition as a potential method for wastewater treatment due to its advantages of minimal secondary pollution, simplicity, repeatability, low cost, and high efficiency compared to other technology [7].

As an effective removal alternative procedure for water purification, photocatalyst, especially heterogeneous ones, has attracted study [8]. The electron/hole (e^-/h^+) pairs, hydroxyl radicals, and superoxide radicals are the four primary reactive species in a heterogeneous

* Corresponding author.
E-mail address: esuharyadi@ugm.ac.id (E. Suharyadi).

https://doi.org/10.1016/j.cscee.2023.100301
Received 26 November 2022; Received in revised form 10 January 2023; Accepted 12 January 2023
Available online 14 January 2023

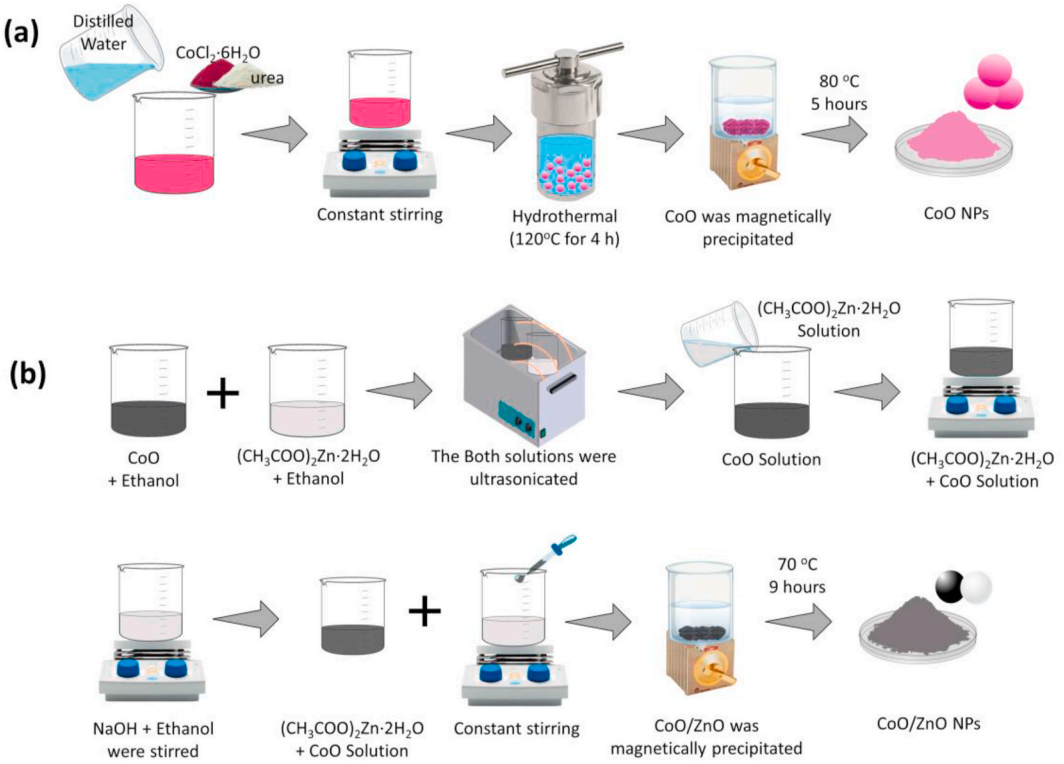

Fig. 1. Synthesis schematic of (a) CoO NPs under hydrothermal method and (b) CoO/ZnO NPs under precipitation method.

photocatalyst. When exposed to UV or visible photons with sufficient energy equal to or higher than the bandgap energy (E_g) of the semiconductor, the e^-/h^+ pairs could be inducted in the conduction (CB) and valence bands (VB) of the suggested semiconductor to generate reactive oxygen species (ROS). The photogenerated VB-holes can react with water or hydroxyl anions to make the hydroxyl radical (*OH), whereas the photo-induced CB-electrons can react with the dissolved oxygen to produce superoxide radicals ($*O^{2-}$). These reactive species attack the examined pollutant molecules in a series that breaks them down into the smaller chemical compound. The investigation pollutant and its degradation products are converted to non-toxic products, such as NO_3^-, SO_4^{2-}, CO_2, and water, as the final objective and step of the heterogeneous photodegradation [9].

Many researchers have used transition metals as catalysts to produce strong degradation performance towards organic pollutants [10,11]. Due to their high degrading efficiency and excellent stability in ROS activation, heterogeneous cobalt-based catalysts (e.g., CoO, Co_3O_4) have attracted growing attention in studies of transition metals as catalysts. Due to their high catalytic oxidation activity, low operating costs with earth abundance, and good environmental compatibility, Co_3O_4 and CoO catalysts are considered appropriate and reactive for treating organic pollutants [12,13]. However, the photocatalytic activity of pure CoO needs to be improved for practical applications due to the high electron-hole recombination rate and low separation efficiency of charge carriers-induced thermal oxidation caused by CoO agglomeration [13]. CoO catalyst can be utilised as a p-type semiconductor to construct a heterojunction photocatalyst [14]. The construction of heterojunction composites generally is a promising and effective method for increasing photocatalytic activity by suppressing charge recombination and broadening the photoexcitation range [15]. Surprisingly, a p-n junction with a built-in electric field is considered an efficient method for enhancing photocatalytic activity by preventing CoO aggregation, limiting charge recombination, and facilitating the separation of photogenerated carriers [16]. Numerous reports of these p-n heterojunctions based on CoO for photocatalytic applications, for instance, $CoO/BiPO_4$ [17], CoO/Bi_2WO_6 [13], CoO/ZnO [14], CoO/TiO_2 [18], CoO/CoS [19].

ZnO is a promising semiconductor for numerous applications, such as photocatalysis in wastewater treatment, due to its chemical stability, high photosensitivity, cost-effective photocatalytic activity, and non-toxicity. ZnO possesses an n-type semiconductor with a direct bandgap energy of approximately 3.3 eV; therefore, it can be applied as a photocatalyst under ultraviolet irradiation and can be affordably reused [20]. Despite these advantages, the application of ZnO in wastewater treatment is severely restricted by the rapid recombination of photo-induced charge carriers and low water stability, which can be related to the $Zn(OH)_2$ formation in aqueous solutions [21]. Fortunately, the addition of n-type ZnO on the surface of the P-type semiconductor allowed for the formation of p-n type heterojunction, which expedited the effective separation of photogenerated carriers and reduced recombination. In particular, Warshagha and Muner [22] decorated n-type ZnO on the surface of p-type CdO to construct a p-n CdO/ZnO heterojunction with excellent photodegradation activity for methylene blue (99.2%, 60 min) and Rhodamin B (98.4%, 100 min) and favourable reusability. Combining n-type ZnO with p-type CoO to form p-n heterostructures can accomplish various goals: (i) promotes the separation of photogenerated carriers, (ii) avoids aggregation via a built-in electric field, and (iii) constructs p-n heterojunction, which allows for effective charge separation, thus improving photocatalytic activity and reusability.

Herein, we systematically synthesized CoO/ZnO p-n heterojunction composite using the precipitation method with various ZnO molar ratios. The microstructure, morphology, optical, and magnetic properties were investigated by a series of characterizations. The photocatalytic activity of the as-synthesized heterojunctions was investigated by degrading methylene blue (MB) as a dye model under UV light irradiation. Photodegradation process was analyzed using the Langmuir-Hinshelwood kinetic model. The pseudo-first-order, coefficient of degradation rate, and half-life of photocatalytic activity degradation were estimated. The correlation coefficient calculation revealed the best

linear relation between the theoretical model and the experimental data collected. Furthermore, the reusability of the CoO/ZnO p-n heterojunction was also discussed in detail.

2. Materials and methods

2.1. Materials

Cobalt (II) chloride hexahydrate ($CoCl_2{\cdot}6H_2O$, purity >99%), urea (CH_4N_2O, analytical grade), zinc acetate dihydrate ($(CH_3COO)_2Zn{\cdot}2H_2O$, >98%), sodium hydroxide pellets (NaOH, >99%), ethanol absolute (CH_3CH_2OH, >99%), MB ($C_{16}H_{18}N_3SCl$), and hydrogen peroxide (H_2O_2, 30%) were obtained from Merck (Darmstadt, Germany) and were used without further purification. Distilled water was used in all the experiment processes.

2.2. Synthesis of CoO NPs

CoO NPs were synthesized through the hydrothermal method, following research by Zang et al. [23]. Simultaneously, 1.76 g $CoCl_2{\cdot}6H_2O$ and 4.4 g CH_4N_2O were dissolved in 60 mL distilled water and stirred for 1 h at room temperature. The above solution was transferred into two separate 50 mL Teflon-lined autoclaves, which were maintained at 120 °C for 4 h and then naturally cooled to room temperature. After the hydrothermal reaction, the precursor was ultrasonically treated for several minutes. The NPs were then magnetically precipitated using an external magnetic field, washed thoroughly with ethanol and distilled water several times, and dried at 80 °C for 5 h. Afterward, the precursor was calcinated in a furnace at 600 °C for 240 minutes at a heating rate of 5 °C min^{-1}, resulting in CoO NPs black powder, as illustrated in Fig. 1(a).

2.3. Synthesis of CoO/ZnO NPs

Fig. 1(b) shows a schematic of the CoO/ZnO NPs synthesis procedure under the precipitation method [24]. CoO and $(CH_3COO)_2Zn{\cdot}2H_2O$ powders were separately dissolved in 53 mL ethanol. Both solutions were ultrasonicated at room temperature for several minutes. $(CH_3COO)_2Zn{\cdot}2H_2O$ was then transferred into CoO to form a new solution and magnetically stirred for several minutes.

Further, the above solution was added dropwise into the NaOH solution and stirred at 66–67 °C for 1 h. The final solution was rinsed multiple times with distilled water and precipitated using an external magnet. The precipitate was then dried at 70 °C for 9 h to obtain CoO/ZnO NPs' greyish-black powder. The CoO/ZnO NPs with the molar ratio of CoO:ZnO equal to 1:1, 1:2, 1:3, 1:4, and 1:5 were synthesized under the same condition. Pure CoO was prepared and did not contain ZnO; meanwhile, pure ZnO was also prepared as CoO/ZnO with a molar ratio of 0:1.

2.4. Characterization

The X-ray diffraction (XRD) of the powders was determined by Shimadzu XD-3H, Cu Kα radiation (λ = 1.5418 Å) to analyze crystal structure and phase formation. The morphology and particle size distribution were evaluated via transmission electron microscopy (TEM, JEOL JEM 1400). The surface morphology was observed using a scanning electron microscope (SEM, JSM-6510LA), which was attached with an Energy Dispersive X-Ray (EDX) to determine the chemical composition distribution of CoO:ZnO NPs in the SEM images. Fourier-transform infrared (FTIR) spectroscopy in the spectra range 400–4000 cm^{-1} was recorded on IR Spectrometer Shimadzu Prestige-21 to analyze the functional groups. The optical properties of NPs were investigated using ultraviolet–visible (UV–vis) spectroscopy (Shimadzu Spectrophotometer UV-1900). The magnetic properties of the NPs were determined using a vibrating sample magnetometer (VSM, Riken Denshi Co. Ltd.).

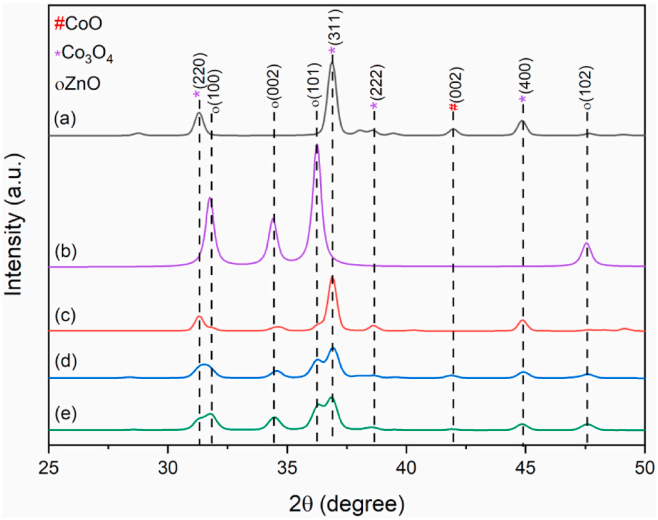

Fig. 2. X-ray diffraction pattern of (a) CoO, (b) ZnO, (c) CoO/ZnO 1:1, (d) CoO/ZnO 1:3, (e) CoO/ZnO 1:5 NPs.

2.5. Photocatalytic activity evaluation

The photocatalytic activities of the CoO/ZnO NPs were examined in aqueous MB. A very little amount of H_2O_2 (0.25 mL) was dropped in MB solution (7 ppm). Photodegradation of MB was accomplished by stirring a mixture containing 0.1 g of catalyst per 100 mL of MB solution while exposed to three UV lights (234 nm, 30 W). Before irradiation, the reaction mixture was stirred in the dark for 30 min to reach adsorption-desorption equilibrium on the surface of CoO/ZnO NPs. There were no significant changes in the MB or redox absorption spectra after stirring in dark conditions. Then, the mixture was magnetically stirred under UV light irradiation for 180 min. MB samples (10 mL) were taken every 30 min, and all samples were left overnight in dark conditions to separate the suspended catalyst from the solution. The degradation kinetics was investigated under UV light. The absorbance of degraded MB was then measured with a UV–vis spectrophotometer. The NPs were washed to remove the MB residual attached to the surface and then dried in a furnace at 80 °C for 2 h. The photocatalytic reusability of CoO/ZnO NPs was investigated under the same treatment. The reused NPs were labeled as R1, R2, and R3, referring to the first, second, and third reuses, respectively.

3. Result and discussion

3.1. Characteristics of nanocomposites

3.1.1. Crystalline structure, morphology, and compositions

XRD patterns of CoO, ZnO, and CoO/ZnO NPs with various ZnO molar ratios were revealed in Fig. 2. MAUD software has done the Rietveld refinement of XRD data, resulting in distinctive peaks without noise [25]. The XRD pattern of the pure CoO NPs showed another phase formed beside the CoO phase, namely the Co_3O_4 phase. The CoO and Co_3O_4 phases are hexagonal and cubic spinel crystal structures, respectively, matching with the standard spectra of CoO (ICDD Card No. 01-089-2803) and Co_3O_4 (ICDD Card No. 00-043-1003) [26,27]. The CoO was oxidized at high temperatures during the calcination process, leading to the Co_3O_4 formation. The presence of Co_3O_4 in the CoO sample is supported by Żyła et al. [28], that there are only two stable cobalt oxides at high temperatures, which are CoO and Co_3O_4. The CoO phase showed several diffraction peaks observed at 2θ angles: 42.0°, which corresponded to the (002) plane [29], while the Co_3O_4 phase showed diffraction peaks at 2θ angles: 31.3°, 36.9°, 38.6°, and 44.8°, which were assigned to the lattice planes (220), (311), (222), and (400)

Table 1
The phase composition, lattice parameter, and average crystallite size of CoO NPs and various molar ratios of CoO/ZnO NPs.

Sample	Phase Composition (%)		Lattice Parameter (Å)				Crystallite Size (nm)
	CoO	ZnO	CoO		ZnO		
			a = b	c	a = b	c	
CoO	86.0	–	2.5	4.39	-	-	21.9 ± 0.3
CoO/ZnO (1:1)	0.01	4.97	2.92	5.05	–	–	21.4 ± 0.1
CoO/ZnO (1:3)	2.60	29.74	2.90	5.02	2.15	3.72	16.8 ± 0.2
CoO/ZnO (1:5)	3.99	36.77	2.91	5.04	2.31	4.01	15.8 ± 0.2

[30]. The characteristic peaks of the ZnO wurtzite hexagonal crystal structure (ICDD Card No. 01-079-0208) were identified in the XRD spectra in Fig. 2(b–d) at 2θ angles: 31.7°, 34.5°, 36.2° 47.7°, representing the lattice planes (100), (002), (101), and (102) [31]. The formation of the CoO, Co_3O_4, and ZnO phases at the XRD spectrum confirmed that CoO NPs and CoO/ZnO NPs had been successfully synthesized.

The best number of phase compositions and lattice parameters obtained from the data on crystal diffraction is required to accomplish the considerable adaptability and excellent performance in Rietveld refinement of the materials [32]. The Gaussian approximation for numerous peaks was used to determine the NPs' crystal size, which was then determined using the Debye-Scherrer equation [33]:

$$D = \frac{k\lambda}{\beta \cos\theta} \quad (1)$$

D, k, and λ are the average crystallite size, Scherrer's constant (crystallite shape factor), and the X-ray beam wavelength, respectively. The terms β and θ denote the full peak width at half maximum (FWHM) and Bragg's diffraction angle, respectively. The refined phase composition, lattice parameters, and crystallite size of pure CoO and CoO/ZnO NPs are presented in Table 1.

The CoO and ZnO's phase composition increased with the ZnO ratios, while the remaining percentage belonged to Co_3O_4. This led to the distinctive peak intensity of CoO (peak at 42.0°) and ZnO gradually strengthening and narrowing. The XRD peaks representing Co_3O_4 exhibited decreasing intensity along with the increasing ZnO ratios, followed by the peak widening and shifting of Co_3O_4 towards a smaller 2θ angle. Unit cell parameters a (Å) and c (Å) of the CoO/ZnO NPs are the combination of the cubic structure ($a = b = c$) of Co_3O_4 and the hexagonal structure ($a = b \neq c$) of CoO and ZnO. The unit cell of the CoO and Co_3O_4 increase with the increasing ZnO. This change in lattice parameters is caused by the interfacial substitution of Zn^{2+} ions in the diffusion layer, filling the space at the CoO and Co_3O_4 sites. It causes peak shifting, increases lattice parameters, and decreases crystallite size in CoO/ZnO NPs. The evaluated unit cell parameter has demonstrated a decent match with Goktas et al. [34]. The shift of peak diffraction also indicates the increased micro-strain on the NPs, allowing the formation of dislocations or lattice defects, such as oxygen vacancy donated from Co^{2+}; therefore, the degree of long-range order and crystallinity will be decreased [34]. After the CoO–ZnO NPs heterostructure formed, the

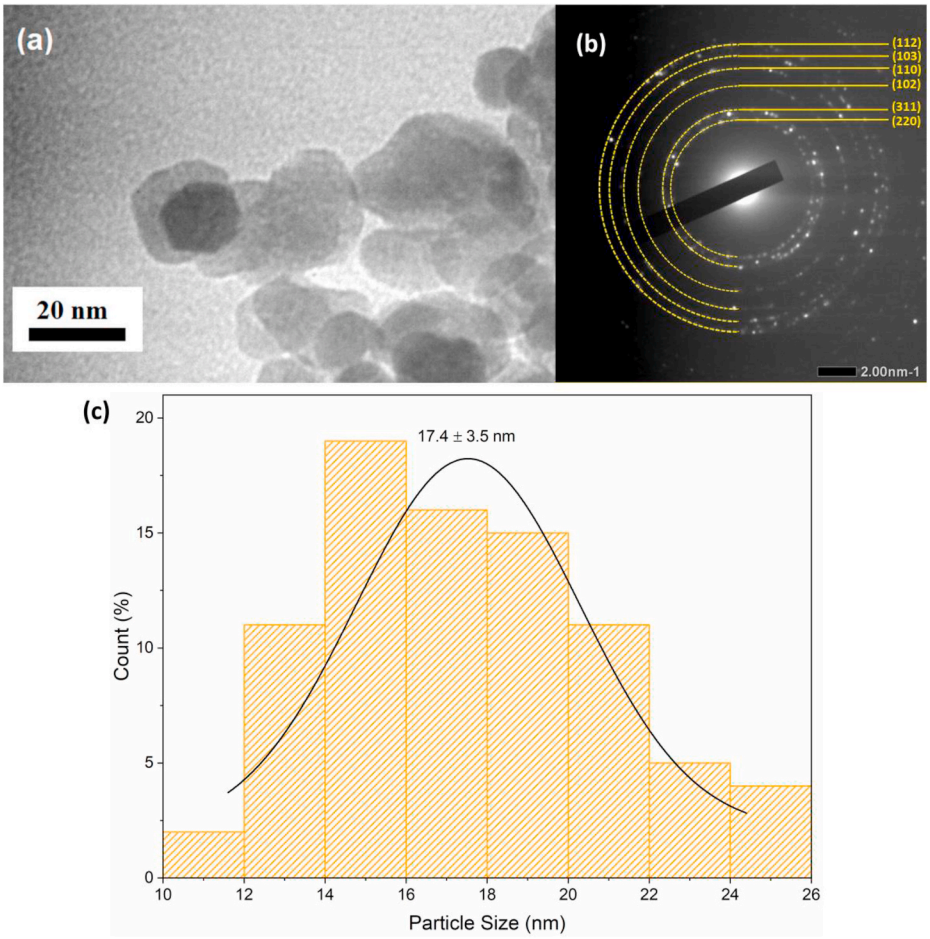

Fig. 3. (a) TEM image; (b) SAED image; and (c) particle size distribution of CoO/ZnO NPs with CoO:ZnO of 1:3.

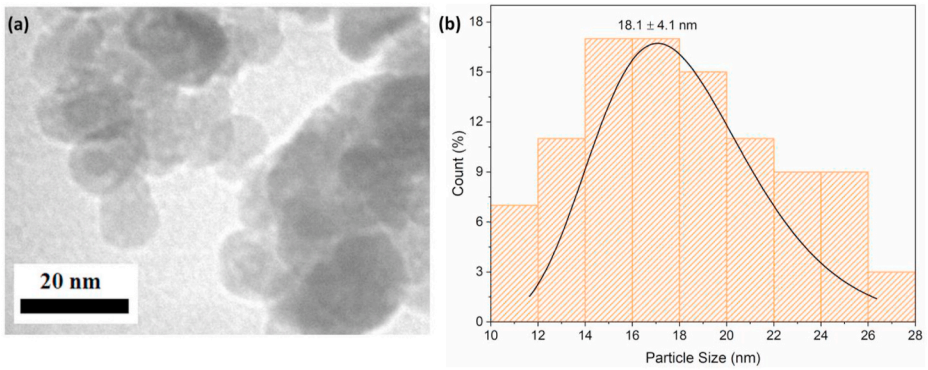

Fig. 4. (a) TEM image and (b) particle size distribution of CoO/ZnO NPs with CoO:ZnO of 1:2.

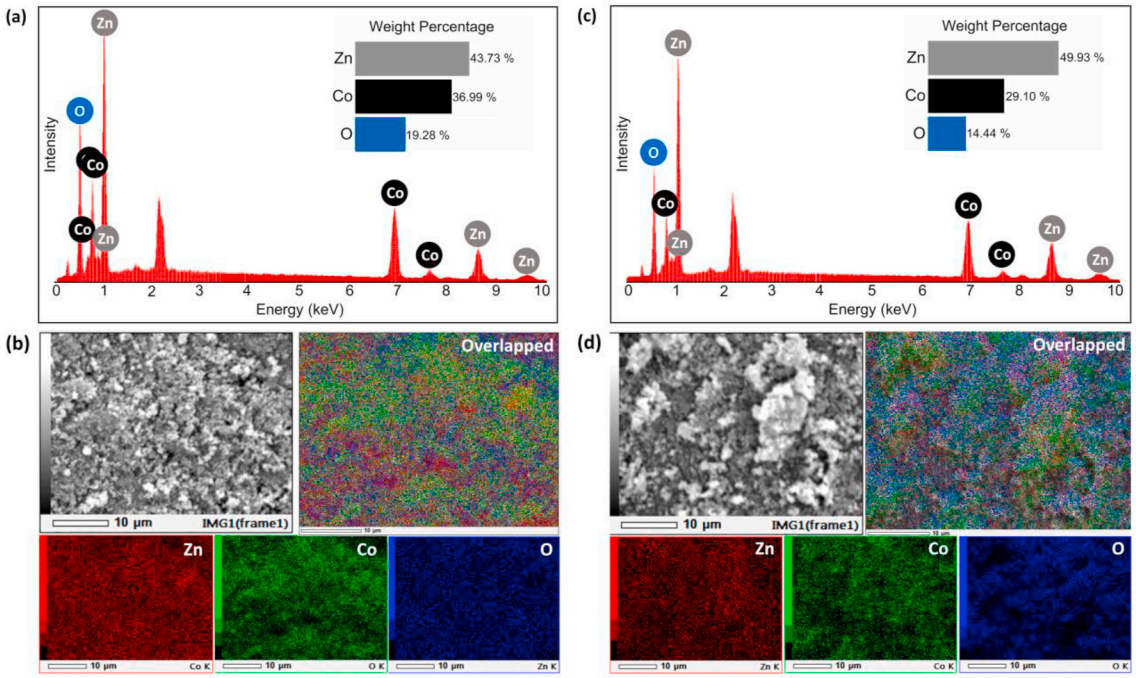

Fig. 5. (a) EDX Spectrum and (b) mapping analysis of the element of CoO/ZnO NPs with CoO:ZnO molar ratio of and 1:2. (c) EDX Spectrum and (d) mapping analysis of the element of CoO/ZnO NPs with CoO:ZnO molar ratio of 1:3.

characteristic peaks of ZnO gradually increased with the increasing molar ratio, indicating that ZnO was successfully decorated on the surface of CoO [35].

Further investigations about the structure and morphology of CoO/ZnO composites were carried out by TEM. Fig. 3(a) and (b) show TEM images of the CoO/ZnO NPs with a molar ratio of 1:3. CoO/ZnO 1:3 composites possess small particles on a nano-scale, approximately 17.4 ± 3.5 nm with non-homogeneous particle size distribution. CoO/ZnO 1:3 NPs have imperfectly spherical and non-uniform particle shapes. Moreover, a small bit of darkness was also dissipated on the rough grey edge, indicating some spheres have somewhat agglomerated [13]. It has been suggested that decorating ZnO on a large specific surface area could prevent serious agglomeration of CoO nanoparticles, consequently exhibiting grain growth. A small particle size denotes a large surface area and optimum bandgap energy, which are advantageous and favourable for photocatalytic application [36]. Fig. 3(c) shows the selected area electron diffraction (SAED) patterns of the CoO/ZnO NPs. The noticed lattice spacing can be ascribed to the lattice plane of (220) and (311) Co_3O_4 spinel cubic, (110) CoO hexagonal, (112), (103), and (102) ZnO wurtzite hexagonal crystalline structures. The SAED pattern of the CoO/ZnO NPs is attributed to the short-range ordering among the unit cells [37]. Hence, the SAED investigation also validated the XRD analyses. The diffraction ring pattern of the CoO/ZnO NPs revealed a polycrystalline combination of different phases: a polycrystal of spinel cubic Co_3O_4 and hexagonal CoO and ZnO phases. The estimation results of the SAED images confirmed appropriate *hkl* lattice spacing in the XRD results. According to the above result, an integrated heterostructure was constructed between CoO and ZnO [14].

Morphology of CoO/ZnO NPs with a molar ratio of 1:2 was shown in Fig. 4. CoO/ZnO 1:2 also have imperfectly spherical and heterogenous particle shape. The particle size was also calculated to be in nano scale, approximately 18.1 ± 4.1 nm, which is bigger than CoO/ZnO 1:3. Less ZnO concentration makes the agglomerated particle looks to be cleaner and broader in CoO/ZnO NPs. This further demonstrates that agglomeration may be prevented by adding ZnO to the CoO/ZnO composite and that agglomeration is unaffected by particle size reduction driven on by an increase in ZnO concentration. ZnO may attach to the surface of CoO, which changes the morphological environment and causes clearer boundaries than pure CoO as reported by Wang et al. [17]. The reduce size of nanocomposites is appropriate with the crystallite size from XRD

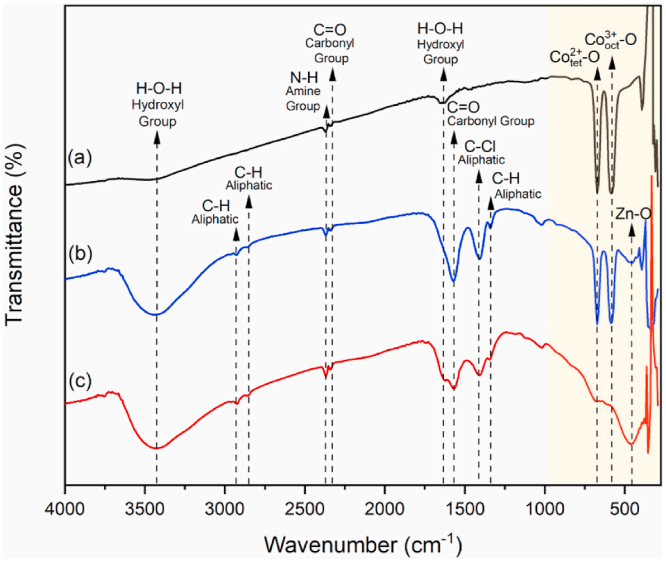

Fig. 6. FTIR spectra of (a) CoO, (b) CoO/ZnO with molar ratio 1:1, (c) ZnO NPs.

analyses.

The composition of chemical elements in the CoO/ZnO NPs were identified using the EDX spectra. Fig. 5 (a) and (c) confirm the elemental composition of the CoO/ZnO sample with a molar ratio of 1:2 and 1:3, respectively. The NPs compositions of 1:2 has a weight percentage of O 19.28%, Co 36.99%, and Zn 43.73%; meanwhile 1:3 has a weight percentage of O 14.44%, Co 29.10%, and Zn 49.93%. The remaining weight percentages belonged to the C atom, emerging due to the experimental treatment. The calculation of both molar ratios was almost equivalent to the stoichiometric of CoO and ZnO. The existence of these elements is consistent with the findings of earlier investigation [38]. The existence of elements O, Co, and Zn in both verified the CoO/ZnO NPs formation. Thereafter, the elemental composition of the CoO/ZnO NPs heterojunction was revealed by EDX elemental mapping in Fig. 5 (b) and (d). The images of the cobalt and zinc distribution by EDX measurements indicate the complete solubility of ZnO in CoO with an increased zinc content. The results proved that Co, Zn, and O were equally distributed and were the primary elements, demonstrating the intimate contact and fine construction of the CoO/ZnO heterojunction [39].

3.1.2. Functional group analyses

The FTIR spectra in the range 400–4000 cm^{-1} for the prepared CoO, ZnO, and CoO/ZnO NPs with a 1:1 M ratio are depicted in Fig. 6. The broad bands at 3441–3487 cm^{-1} and 1626–1635 cm^{-1} were attributed to the peak of the H–O–H stretching and H–O–H bending vibration (hydroxyl group), respectively. The H–O–H peak confirms that water molecules were still adsorbed on the surfaces of CoO, ZnO, and CoO/ZnO NPs, due to insufficient drying [40]. 2841-2931 cm^{-1} and 1334-1342 cm^{-1} peaks are due to asymmetric and symmetric C–H stretching and C–H bending (aliphatic), respectively. The bands at 2368, 2337, 1568, 1573, and 1400 cm^{-1} belong to -N–H stretching (amine group), asymmetric and symmetric C = O stretching, C= C bending in alkene, C–Cl stretching, respectively, from various dangling bonds formed on the surface of NPs [41]. The absorption bands at 671 cm^{-1} and 586 cm^{-1} correspond to the stretching vibration of the C^{2+}_{tet}-O bonds at tetrahedral sites and C^{3+}_{oct}-O bonds at octahedral sites. This only happens if the tetrahedral cation-oxygen bonds are stronger or at least of the same magnitude as the octahedral cations-oxygen bonds. The valency of tetrahedral cations must be greater than that of octahedral cations [42]. The presence of the Co^{3+} cation in XRD data supports the existence of the Co_3O_4 phase because Co_3O_4 has the empirical formula $CoCo_2O_4$ with the forming ions Co^{2+} and Co^{3+} [43,44]. The ZnO and CoO/ZnO NPs also show vibrational bands at 462 and 455 cm^{-1}, respectively, corresponding to Zn–O bonds [45,46]. The shift in wavenumber implies that ZnO influences the connection between metal ions, causing it to weaken. When CoO NPs are combined with ZnO, the vibrational energy between the bonds reduces, resulting in a vibrational shift. The shift in wavenumber, peak shape, and intensity suggest morphological changes in CoO/ZnO NPs [47]. The distinctive vibration peaks of the CoO and ZnO in the CoO/ZnO sample indicate that the CoO/ZnO NPs were successfully synthesized.

3.1.3. Optical properties

The optical properties of as-synthesized CoO, ZnO, and CoO/ZnO NPs were conducted by UV–vis absorption. Fig. 7 (a) displays the UV–vis absorbance spectra of the CoO, ZnO, and CoO/ZnO NPs. The NPs had light absorption ability at 190–350 nm wavelength in the UV–Visible region. The pure CoO and ZnO NPs had the maximum absorption peak at 193.9 and 194.3 nm, respectively, which possed strong light absorption in ultraviolet regions. However, the absorption edge of CoO/ZnO NPs with the increasing ZnO content was gradually shifted to a longer wavelength (redshift) while still exhibiting substantial UV light absorption. The maximum absorption of CoO/ZnO with various ZnO molar ratios of 1:1, 1:2, 1:3, 1:4, and 1:5 were 195.1, 194.3, 194.0, 194.0, and 194.0 nm, respectively. The increasing wavelength gradually narrowed the absorption edge, which matched the previous report [14]. However, when the molarity ratio of CoO/ZnO increased to 1:2, 1:3, 1:4, and 1:5, the absorption peaks resembled the ZnO absorption edge. The phenomena happened as a result of the CoO's capacity to extend the energy range of the ZnO CB at the two-phase interface, which resulted in energy level quantisation and a shift in the UV absorption band [48].

The absorption spectra were then converted using the Tauc plot

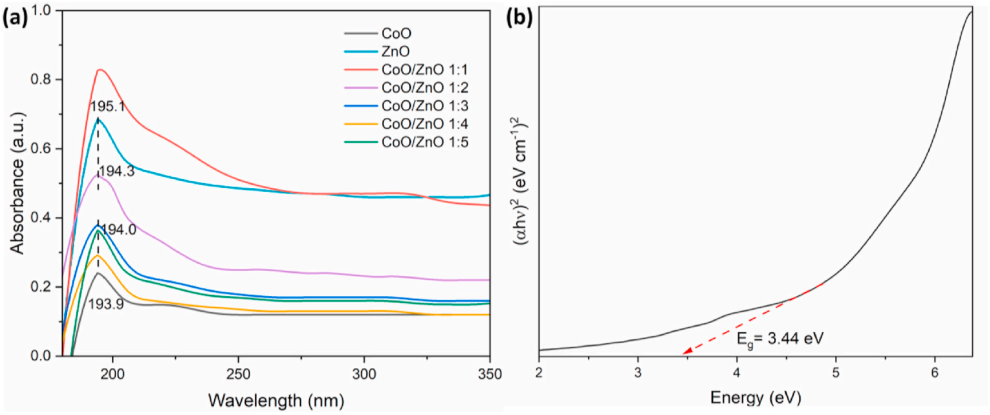

Fig. 7. UV–Vis Absorption of CoO and CoO/ZnO and (b) Tauc plot of the Kubelka—Munk function (direct) for CoO/ZnO NPs with CoO:ZnO molar ratios of 1:1.

Table 2
Bandgap energy of CoO, ZnO, and CoO/ZnO NPs with various molar ratios.

Sample	Maximum absorption (nm)	Bandgap Energy (eV)
CoO	193.9	4.28 ± 0.01
ZnO	194.3	3.30 ± 0.01
CoO/ZnO 1:1	195.1	3.44 ± 0.01
CoO/ZnO 1:2	194.3	3.30 ± 0.02
CoO/ZnO 1:3	194.0	3.20 ± 0.01
CoO/ZnO 1:4	194.0	3.16 ± 0.01
CoO/ZnO 1:5	194.0	3.14 ± 0.02

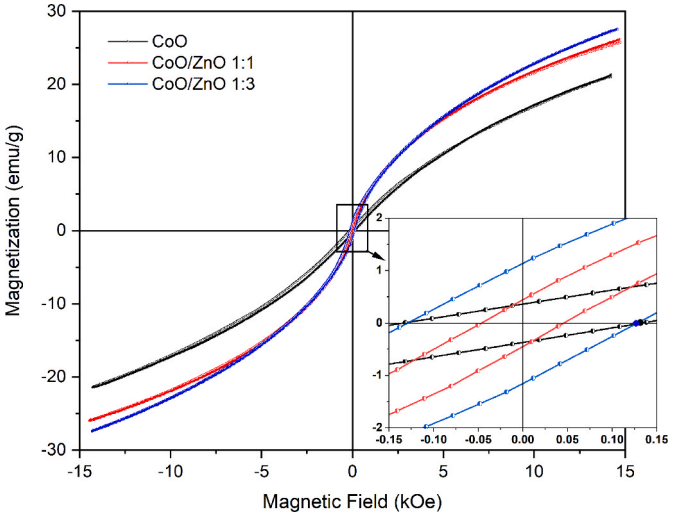

Fig. 8. Hysteresis loop of CoO NPs and CoO/ZnO NPs with various molar ratios.

equation to estimate the bandgap energy (E_g) of the CoO, ZnO and CoO/ZnO NPs [49],

$$(\alpha h\nu)^n = A(h\nu - E_g) \quad (2)$$

α, $h\nu$, A, n are the absorption coefficient, discrete photon energy, a constant relative to material, and an exponent value relative to the transition type ($n = 2$ for indirect transition, 3/2 for a direct forbidden gap, and 1/2 for direct transition), respectively. A plot of $(\alpha h\nu)^2$ against $h\nu$ affords a curve and extrapolated linear region, resulting $h\nu$ value at $\alpha = 0$ and providing absorption edge energies corresponding to the Eg as shown in Fig. 7 (b). The estimated E_g values of CoO, ZnO, and CoO/ZnO NPs with various molar ratios are present in Table 2.

The CoO and ZnO NPs showed bandgap energy of 4.28 ± 0.01 and 3.30 ± 0.01 eV, respectively. The obtained ZnO bandgap energy is in agreement with the previous research. Sansenya et al. [50] reported that ZnO NPs have an optical bandgap of 3.3 eV. Meanwhile, the optical bandgap of CoO NPs didn't match the previous research, in which the bandgap energy should be 2.28 eV [51]. The optical properties of CoO NPs distinguish significantly due to the appearance of Co_3O_4 cubic spinel structure with Eg 3.95 eV, inducing the change E_g to higher energy [52]. Moreover, the change of E_g of CoO NPs was also affordably affected by the calcination of the CoO at high temperatures. Siva, Ranga, and Nageswara [53] revealed that high-temperature calcination results in a wider band gap and larger bandgap energy. The band gap values for the various molar ratio of CoO/ZnO were 3.44 ± 0.01, 3.30 ± 0.02, 3.20 ± 0.01, 3.16 ± 0.01, and 3.14 ± 0.02 eV, which correspond to molar ratios of 1:1; 1:2; 1:3; 1:4; and 1:5, respectively. The bandgap energy of CoO/ZnO NPs was reduced with increasing ZnO content, which was attributed to the new bandgap formation. The Zn^{2+} ions incorporation into Co^{3+} or Co^{2+} at the interface had been proved to cause redshift, forming Co–O–Zn bonds on the surface. The bond formation causes

Table 3
Coercivity (H_c) of CoO NPs and CoO/ZnO NPs with various ratio molar.

Sample	H_c (Oe)
CoO	133
CoO/ZnO 1:1	47
CoO/ZnO 1:3	131

electron deficiency in the ZnO structure, leading to a new bandgap located below and adjacent to the CoO conduction band [54]. The above results verify that the semiconductors p-type CoO and n-type ZnO satisfy the required requirements for constructing a p-n heterojunction; thus, photocatalytic activity can be exceedingly reactive when CoO/ZnO is exposed under UV light.

3.1.4. Magnetic properties

The magnetic properties of CoO and CoO/ZnO NPs with varied molar ratios of 1:1 and 1:3 were investigated using a VSM in an external magnetic field (between −15 kOe and +15 kOe), as shown in Fig. 8. The narrow hysteresis loop shows that the NPs tend to have soft-magnetic properties. The magnetisation of CoO, CoO/ZnO (1:1), and CoO/ZnO (1:3) continue to rise even at H = 15 kOe; hence NPs did not undergo saturation magnetisation. Barman et al. [55] reported that CoO had stable antiferromagnetic properties at room temperature. Ferromagnetic behaviour in CoO nanocrystals is commonly identified with a crystallite size of less than 10 nm [56]. However, since the crystal size of CoO and CoO/ZnO NPs investigated were around 16–22 nm, that may produce a magnetic disorder or uncompensated spins; therefore, their magnetic properties tend to be antiferromagnetic [57]. Antiferromagnetic on CoO and CoO/ZnO NPs reveal that the exchange coupling of magnetic moments in CoO/ZnO was inadequate due to lattice defects. The defects in the crystal structure cause a change in the ion's location and bond lengths between cations and anions in the crystal lattice, which affect the magnetic interactions [43].

The inserted graph in Fig. 8 demonstrates the intersection of the magnetic field axes, revealing the coercivity (H_C) of the samples that are presented in Table 3. The H_C of CoO/ZnO NPs increased with the increasing ZnO, leading to anisotropic energy, though the H_C of CoO/ZnO was still lower than that of pure CoO [58]. This magnetic behaviour agrees with the XRD spectrum, which exhibits the shifting diffraction peaks, the increasing lattice parameter, and the decreasing crystallite size, suggesting substantial surface-disorder effects. Therefore, these results allow us to figure out that the NPs present a high spins degree and crystal surface disorder.

3.2. Photocatalytic activity and mechanism

The photocatalytic activities of the CoO and CoO/ZnO NPs were estimated against the photodegradation on MB aqueous under UV light irradiation. MB was used as the dye model to investigate the photodegradation activity of the CoO/ZnO NPs composite. Fig. 9 shows that the dark absorption equilibrium is established after 30 min. Photodegradation of MB was investigated using CoO/ZnO NPs with a molar ratio of 1:2, as it resulted in maximum photodegradation activity compared to pure CoO and other variations of ZnO molar ratios. The NPs showed excellent adsorption properties, as shown in Fig. 9. The highest absorbance of MB, which corresponds to the distinctive absorption peak of MB at 664 nm, steadily declined with increasing UV irradiation period. The samples were subsequently exposed to UV radiation for 180 minutes.

The CoO/ZnO NPs (1:2) showed significant degradation in the MB solution (Fig. 9 (a)). Therefore, the photocatalytic activity of the nanocomposite may be significantly increased with a proper loading amount of ZnO. This can be attributable to the following factors: (1) when the loading quantity of ZnO was less than CoO/ZnO 1:2, the synergistic

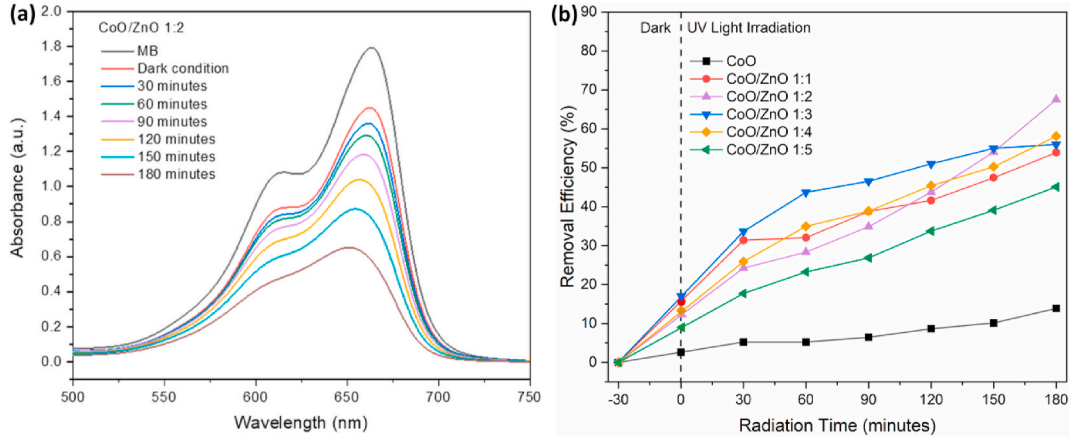

Fig. 9. (a) UV–Vis absorption spectrum for MB degradation using CoO/ZnO NPs 1:2 and (b) removal efficiency of MB using CoO NPs and various molar ratios of CoO/ZnO NPs.

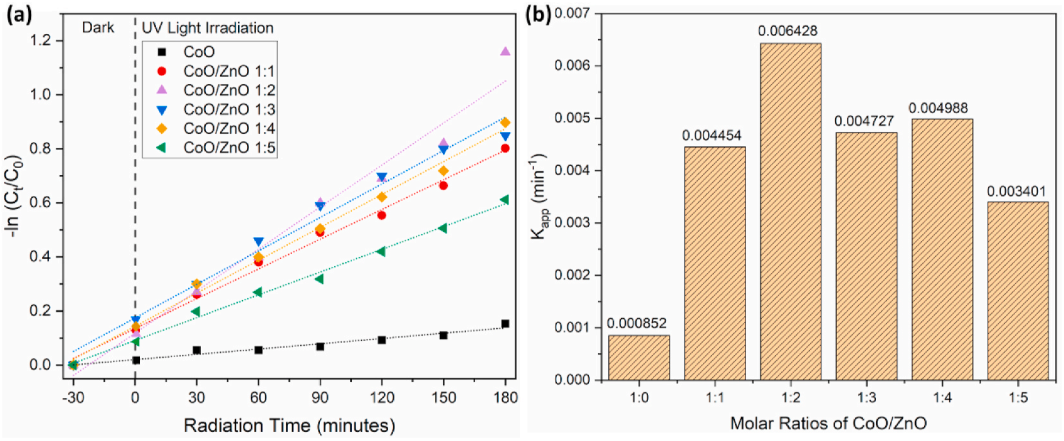

Fig. 10. (a) Pseudo-first-order kinetic model and (b) rate constant of MB photodegradation for CoO and CoO/ZnO NPs with various molar ratios.

impact between the ZnO and CoO was insufficient, which reduced charge carrier migration. (2) When the loading amount of ZnO exceeded the CoO/ZnO 1:2 ratio, the active sites of CoO were extensively shielded by excess ZnO, becoming charge carrier recombination centers. All of these findings coincided with the charge carrier dynamics analyses of the nanocomposites [59]. The CoO/ZnO NPs have excellent performance in the MB degradation under UV irradiation due to certain containing ZnO on the CoO surface. This phenomenon proves that ZnO plays an essential role in the adsorption process. The removal efficiency (D) or de-colouration rate was calculated using the following equation [7]:

$$D\ (\%) = \frac{C_0 - C_t}{C_0} \times 100 \tag{3}$$

C_0 and C_t represent the initial MB absorbance and the absorbance with specific time radiation. Fig. 9 (b) shows the calculated removal efficiency of the MB after photocatalytic reaction using CoO/ZnO NPs. The deterioration rate increased with increasing UV irradiation period. Under dark circumstances, the adsorption rates of NPs were 4.0%, 27.7%, 19.1%, 29.9%, 22.5%, and 12.8% for CoO/ZnO molar ratios of 1:0, 3:1, 1:1, 1:3, 1:5, and 1:7. After 3h of UV light irradiation, the degradation rate at a molar ratio of 1:0, or without ZnO addition, reached 13.9% or approximately three that of the adsorption process, meanwhile for the CoO/ZnO NPs with a molar ratio of 1:2, the MB removal efficiency reached 67.5% (optimal photodegradation).

As shown in Fig. 10 (a), the photocatalytic MB degradation experiments with NPs of various CoO/ZnO NPs molar ratios were analyzed using kinetic models to investigate the mechanisms that control the degradation process. The rate constant can be determined using the pseudo-first-order reaction rate model (according to the Langmuir–Hinshelwood model), which can be calculated in the following equation [60]:

$$\ln\frac{C_t}{C_0} = -K_{app}t \tag{4}$$

K_{app} and t are the fitted pseudo-first-order model rate constant (min^{-1}) and t the radiation time, respectively. As shown in Fig. 10 (b), the calculated rate constant (Kapp) is present in Table 4. The CoO/ZnO NPs 1:2 catalyst exhibited the highest rate constant (6.43 ± 0.01 min^{-1}), which corresponded to the optimum removal efficiency of CoO/ZnO NPs. The CoO/ZnO with a concentration of 1:2 exhibited the highest degradation rate. The kinetic fitting of experimental data confirmed that

Table 4
Parameters of the pseudo-first-order adjusted for the photocatalytic degradation rate of MB using CoO/ZnO photocatalyst with various molar ratios.

Photocatalyst CoO/ZnO	K_{app} (× 10^{-3}, min^{-1})	$t_{1/2}$ (min)
1:0	0.85 ± 0.01	813.77 ± 0.01
1:1	4.45 ± 0.02	155.63 ± 0.02
1:2	6.43 ± 0.01	107.84 ± 0.01
1:3	4.73 ± 0.12	146.64 ± 0.12
1:4	4.99 ± 0.01	138.96 ± 0.01
1:5	3.40 ± 0.01	203.82 ± 0.01

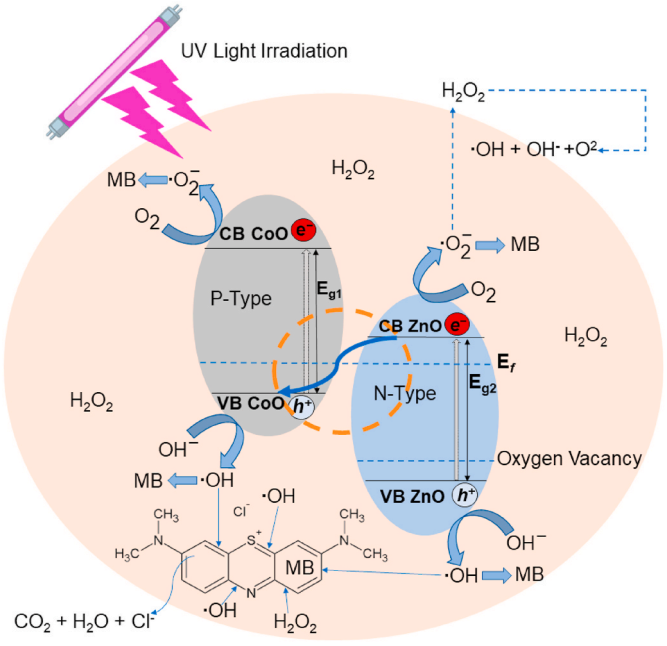

Fig. 11. Simplified Z-scheme depicting electron-hole and band alignment arrangement at the junction of CoO/ZnO NPs with low H_2O_2 concentration addition for MB degradation.

the photocatalysis matched a pseudo-first-order kinetic model with sufficient linearity. Kinetic studies can also be performed to determine the half-life times ($t_{1/2}$) of the MB degradation using the following equation [61]:

$$t_{\frac{1}{2}} = \frac{\ln 2}{K_{app}} \tag{5}$$

K_{app} is inversely proportional to $t_{1/2}$. The smallest K_{app} takes the most prolonged half-life in degrading MB solution. The K_{app} and $t_{1/2}$ of photocatalytic activity performance using CoO and CoO/ZnO NPs with various molar ratios are present in Table 4.

Regarding overall photodegradation results, CoO/ZnO NPs outperformed pure CoO NPs in degrading 7 ppm MB. It is also possible that CoO/ZnO has slightly better degradation than pure ZnO. According to research by Mohammadzadeh et al., ZnO with the addition of 0.2 mL H_2O_2 was able to degrade 91% of 1.2 ppm MB for 150 minutes [62]. In addition to the duration of light irradiation and light intensity, pH conditions can influence the photodegradation rate. MB is a cationic dye; therefore, the photocatalytic process is more active at specific pH levels [63]. The possible photocatalytic mechanism of CoO/ZnO in degrading aqueous MB is depicted in Fig. 11. The photocatalytic activity of CoO/ZnO nanoparticles with the structure of the p-n junction band due to coupling between the CoO band and the ZnO band with the depletion area of the layer where electron transfer is located is illustrated as shown in Fig. 11 [64]. When CoO/ZnO nanoparticles are dissolved into MB solution and given UV light radiation as an energy source, electron-hole pair photogeneration occurs due to the electron excitation process. The electrons (e^-) in the valence band (VB) of each CoO and ZnO are excited to the conduction band (CB) of each CoO and ZnO, respectively and leave a positive charge hole (h^+) in the CB of ZnO. The e^- in the CB of CoO and ZnO then interacts with water molecules, thus undergoing a reduction process with oxygen and generating superoxide radicals ($\bullet O^{2-}$). Meanwhile, h^+ in VB of CoO and ZnO interact with water molecules and then undergo oxidation with OH^- ions from H_2O and H_2O_2 to form hydroxyl radicals (•OH).

However, the Z-scheme nanocomposite could be formed, as reported by previous studies [40,59]. Therefore, the e^- in CB of ZnO might

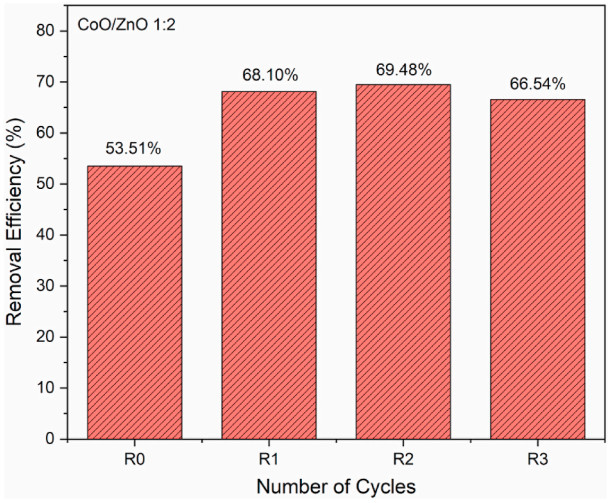

Fig. 12. Experimental results for reusable CoO/ZnO NPs with CoO:ZnO molar ratios of 1:2 used as photocatalysts for MB solution (0.1 g/100 mL) after 3 h of UV irradiation.

recombine with the h^+ in the VB of CoO. This charge carrier migration surmounted the electron-hole pair recombination and granted substantial redox ability in the isolated systems. The stronger reduction ability of e^- in the CB of ZnO can photodegrade the MB, and a certain e^- in the conduction band can interact with O_2 and H^+ to generate H_2O_2. Moreover, it is distinctly noticed that the conduction band of the CoO sample is more positive than that of ZnO. Yet, the valence band of CoO is more negative than that of ZnO [60], suggesting that the generation of $\bullet O^{2-}$ was thermodynamically prohibited. Meanwhile, the accumulated h^+ in VB of ZnO oxidized OH^- and H_2O to form •OH, which is efficient in MB photodegradation [59,65]. The radical species ($\bullet O^2$- and •OH) resulting from the oxidation-reduction process then interact with the MB molecule and remove the MB molecular chain up to a simple single-ring molecular chain that is environmentally friendly, such as H_2O, Cl^-, CO_2, SO_4^{2-}, and NO^{3-}. Under photocatalytic conditions, when low H_2O_2 concentration was added, a high rate of ROS was generated, resulting from the surface binding between CoO and ZnO that matches well with the previous report [66]. The scheme of the photocatalytic reaction of CoO/ZnO NPs is outlined as follows:

$$CoO\,/\,ZnO + hv\ (UV) \rightarrow CoO\left(e_{CB}^- + h_{VB}^+\right)/\,ZnO\left(e_{CB}^- + h_{VB}^+\right)$$

$$h_{VB}^+ + H_2O \rightarrow H^+ + OH^-$$

$$h_{VB}^+ + OH^- \rightarrow \bullet OH\ (\text{oxidation})$$

$$e_{CB}^- + H_2O + H^+ \rightarrow H_2O_2 + O_2$$

$$e_{CB}^- + O_2 \rightarrow \bullet O_2^-\ (\text{reduction})$$

$$O_2^- + H^+ \rightarrow \bullet OOH$$

$$2 \bullet OOH \rightarrow O_2 + H_2O_2$$

$$H_2O_2 + \bullet O_2^- \rightarrow \bullet OH + OH^- + O_2$$

$$\bullet O_2^- + \bullet OH + MB \rightarrow H_2O + O_2 + Cl^- + NO_3^- + CO_2 + SO_4^{2-}$$

Reusability may demonstrate the stability of photocatalysts for environmental remediation systems. The CoO/ZnO NPs with a molar ratio of 1:2 confirm high stability and reusability until the third is reusable, as shown in Fig. 12. The mass of the photocatalyst decreased by 40% (0.04 g) in the first cycle of repeated use and by 10% (0.01 g) in each subsequent cycle due to washing and drying. The photocatalytic

Table 5
Comparison of CoO/ZnO with various synthesis methods and photocatalytic treatment.

Synthesis method	Photocatalytic Treatment	Degradation	References
Precipitation, composite, varying CoO concentration	Visible beam, light irradiation for 2 h, 100 ppm 50 mL MB, pH 10, catalyst 0.05 g.	The MB degradation reached 96% within 2h and no reusability.	[14]
Precipitation, doping, varying Co content	Visible beam, light irradiation 2 h, 100 ppm 50 mL MO, pH 10, catalyst 0.5 g.	The photocatalytic result showed 93% degradation of MO for 2h and three-time reusability.	[67]
Ammonia evaporation, composite, varying Co concentration	UV (200 W tungsten), 1h irradiation, 15 ppm 70 mL MB, catalyst 0.2 g.	The removal efficiency of MB is approximately 80% for 1h and has no reusability.	[46]
Grinding commercial material, composite, Co_2O_3–ZnO	UV (125 W, mercury lamp), 1h irradiation, 5 ppm 100 mL crystal violet dye, catalyst 0.15g.	The photocatalytic activity exhibited 90% in degrading crystal violet for 1h and no reusability.	[68]
Precipitation and hydrothermal, composite, Co doping in ZnO/ZnO films	UV (2 × 8W Osaka UV lamps), 3h irradiation, 10 ppm 70 mL MB, 6 films.	The MB photodegradation showed 60% with Co:ZnO film and 68% with Co:ZnO/ZnO film in 3 h, which was very similar to the result of this study, but no reusability was reported.	[34]
Hydrothermal and Precipitation, composite, varying ZnO concentration	UV beam, 3h irradiation, 7 ppm 100 mL MB, pH 6 catalyst 0.1 g.	CoO/ZnO NPs composites had a degradation ability of MB reached 67.5% within 3h UV irradiation and three-time reusability with the increasing photodegradation activity.	This study

ability was increased in R1 by 14.6% (53.5–68.1%), R2 by 1.4% (69.5–68.1%), and then reduced in R3 by 3.0% (69.5–66.5%). This suggests that the catalyst was recyclable. The reduction in photocatalytic activity of NPs can be attributed to numerous variables, including: (1) The amount of mass reduces throughout washing and drying, resulting in smaller dosages in the following cycle [40]. (2) Catalyst surface activity steadily declines after each cycle due to catechols and intermediates blocking pores and active sites [59]. The effect of mass reduction on the increase in removal MB efficiency is caused by reduced agglomeration particles covering the active side on the surface of CoO/ZnO nanoparticles so that their degradation activity becomes more excellent [13]. A decrease in degradation activity after a third repeated use may result from photocatalyst inactivation due to dye molecules attached to the photocatalyst surface [40]. These findings suggest that CoO/ZnO photocatalysts have the potential to be used repeatedly in the process of degradation of dye pollutants. Table 5 shows previous studies of CoO–ZnO with different synthesis methods and photocatalytic treatment. The combination of CoO and ZnO encourages excellent photocatalytic activity by constructing the P–N junction.

4. Conclusion

CoO/ZnO NPs composites were successfully synthesized by combining CoO and ZnO to construct p-n heterojunction using the hydrothermal method, followed by the calcination, synthesis was then continued under the precipitation method. The particle size was confirmed under nano-scale. The crystallite size and band gap energy were reduced with increasing ZnO concentration. CoO/ZnO NPs had antiferromagnetic properties. The photocatalytic activities of CoO/ZnO were confirmed by MB photodegradation with a maximum removal efficiency of 67.5%. The CoO/ZnO NPs may absorb light in the UV–Vis region between 190 and 350 nm due to their wide absorption edge. Therefore, the CoO/ZnO NPs composite is a highly promising photocatalyst to be developed for environmental applications.

Author contributions

Nugraheni Puspita Rini: Conceptualization, designed the experiments, performed the experiments and collected the data, validation, writing, and original draft preparation. **Nurul Imani Istiqomah:** designed the experiments, performed the experiments, and validation. **Sunarta:** Supervision for SEM-EDX analyses. **Edi Suharyadi:** Conceptualization, validation, review and editing, supervision, funding acquisition, project administration.

Fundings

This work was partly supported by the grant of the Faculty of Mathematics and Natural Science (FMIPA), Universitas Gadjah Mada, the Ministry of Education, Culture, Research and Technology (Republic of Indonesia).

Declaration of competing interest

The authors declare that they have no known competing financial interests or personal relationships that could have appeared to influence the work reported in this paper.

Data availability

Data will be made available on request.

Acknowledgements

The authors would like to thank Prof. Takeshi Kato (Institute of Materials and Systems for Sustainability, Nagoya University, Nagoya, Japan) and Dr. Daiki Oshima (Department of Electronics, Nagoya University, Nagoya, Japan) for their advice, facility access in their laboratory for using vibrating sample magnetometer (VSM, Riken Denshi Co., Ltd.).

References

[1] S. Paul, R. Pegu, S. Das, K.H. Kim, S.S. Bhattacharya, Eco-geological consequences of textile processing wastes: risk assessment, elemental dissolution kinetics, and health hazard potential, Environ. Res. 216 (P4) (2023), 114693, https://doi.org/10.1016/j.envres.2022.114693.
[2] P. Olusakin, T. Oladiran, E. Oyinkansola, O. Joel, Results in Engineering Methylene blue dye : toxicity and potential elimination technology from wastewater, Results Eng. 16 (September) (2022), 100678, https://doi.org/10.1016/j.rineng.2022.100678.
[3] A. Tkaczyk, K. Mitrowska, and A. Posyniak, "Synthetic organic dyes as contaminants of the aquatic environment and their implications for ecosystems : a review," Sci. Total Environ., vol. 717, p. 137222, doi: 10.1016/j.scitotenv.2020.137222.
[4] K. Wu, M. Shi, X. Pan, J. Zhang, X. Zhang, T. Shen, Y. Tian, Enzyme and Microbial Technology Decolourization and biodegradation of methylene blue dye by a ligninolytic enzyme-producing Bacillus thuringiensis : degradation products and pathway, Enzym. Microb. Technol. 156 (January) (2022), 109999, https://doi.org/10.1016/j.enzmictec.2022.109999.
[5] C. Chen, J. Liu, H. Wu, J. Wang, J. Cheng, Roles of coal gasification wastewater in coal electrolysis for hydrogen production, Fuel 305 (April) (2021), 121600, https://doi.org/10.1016/j.fuel.2021.121600.
[6] A.M. Nasir, N.A.H. Nordin, P.S. Goh, A.F. Ismail, Application of two-dimensional leaf-shaped zeolitic imidazolate framework (2D ZIF-L) as arsenite adsorbent :

kinetic , isotherm and mechanism, J. Mol. Liq. 250 (2018) 269–277, https://doi.org/10.1016/j.molliq.2017.12.005.
[7] R. Kumar, S.S. Bahera, K.R. Singh, S. Mishra, B. Panigrahi, T.R. Sahoo, P.K. Parhi, Journal of Photochemistry & Photobiology A : chemistry Biosynthesized gold nanoparticles as photocatalysts for selective degradation of cationic dye and their antimicrobial activity, J. Photochem. Photobiol. Chem. 400 (June) (2020), 112704, https://doi.org/10.1016/j.jphotochem.2020.112704.
[8] R.K. Singh, S. Mishra, S. Jena, B. Panigrahi, B. Das, R. Jayabala, P.K. Parhi, D. Mandal, Rapid colorimetric sensing of gadolinium by EGCG-derived AgNPs: the development of a nanohybrid bioimaging probe, Chem. Commun. 54 (32) (2018) 3981–3984, https://doi.org/10.1039/c8cc01777h.
[9] W. Liu, S. Wang, J. Wang, B. Zhang, L. Liu, H. Liu, J. Yang, Supercritical hydrothermal synthesis of nano-zinc oxide: process and mechanism, Ceram. Int. 48 (16) (2022) 22629–22646, https://doi.org/10.1016/j.ceramint.2022.05.094.
[10] G. Panthi, K.R. Gyawali, M. Park, Towards the enhancement in photocatalytic performance of Ag_3PO_4 nanoparticles through sulfate doping and anchoring on electrospun nanofibers, Nanomaterials 10 (May 2020) (2020) 929, https://doi.org/10.3390/nano10050929.
[11] A. Haruna, I. Abdulkadir, S.O. Idris, Synthesis, characterization and photocatalytic properties of $Bi_{0.85-x}M_xBa_{0.15}FeO_3$ (M = Na and K, X = 0, 0.1) perovskite-like nanoparticles using the sol-gel method, J. King Saud Univ. Sci. 32 (1) (2020) 896–903, https://doi.org/10.1016/j.jksus.2019.05.005.
[12] R. Selvarajan, S. Vadivel, A. Saranya, P. Baraneedharan, R. Jayavel, Facile synthesis of rGO@CoO nanocomposites electrode material for photocatalytic hydrogen generation and supercapacitor applications, Inorg. Chem. Commun. 139 (January) (2022), 109345, https://doi.org/10.1016/j.inoche.2022.109345.
[13] C. Lu, D. Yang, L. Wang, S. Wen, D. Cao, C. Tu, L. Gao, Y. Li, Y. Zhou, W. Huang, Facile construction of CoO/Bi_2WO_6 p-n heterojunction with following Z-Scheme pathways for simultaneous elimination of tetracycline and Cr(VI) under visible light irradiation, J. Alloys Compd. 904 (2022), 164046, https://doi.org/10.1016/j.jallcom.2022.164046.
[14] M. Saeed, M. Adeel, I. Khan, N. Akram, M. Muneer, Synthesis of p-n CoO-ZnO heterojunction for enhanced visible-light assisted photodegradation of methylene blue, New J. Chem. 5 (2021), https://doi.org/10.1039/D1NJ05633F, 0–24.
[15] S. Dash, S. Das, M.I. Khan, S. Sinha, B. Das, R. Jayabalan, P.K. Parhi, S.K. Tripathy, Sonochemically synthesized Ag/$CaCO_3$ nanocomposites : a highly efficient reusable catalyst for reduction of 4-nitrophenol, Mater. Chem. Phys. 220 (September) (2018) 409–416, https://doi.org/10.1016/j.matchemphys.2018.09.019.
[16] Y. Zhao, X. Linghu, Y. Shu, J. Zhang, Z. Chen, Y. Wua, D. Shan, B. Wang, Classification and catalytic mechanisms of heterojunction photocatalysts and the application of titanium dioxide (TiO_2)-based heterojunctions in environmental remediation, J. Environ. Chem. Eng. 10 (3) (2022), 108077, https://doi.org/10.1016/j.jece.2022.108077.
[17] S. Wang, L. Zhao, W. Huang, H. Zhao, J. Chen, Q. Cai, X. Jiang, C. Lu, Solvothermal synthesis of CoO/$BiVO_4$ p-n heterojunction with micro-nano spherical structure for enhanced visible light photocatalytic activity towards degradation of tetracycline, Mater. Res. Bull. 135 (November 2020) (2021), 111161, https://doi.org/10.1016/j.materresbull.2020.111161.
[18] A.K.P.D. Savio, J. Fletcher, K. Smith, R. Iyer, J.M. Bao, F.C. Robles Hernández, Environmentally effective photocatalyst CoO-TiO_2 synthesized by thermal precipitation of Co in amorphous TiO2, Appl. Catal. B Environ. 182 (2016) 449–455, https://doi.org/10.1016/j.apcatb.2015.09.047.
[19] X. Liu, Q. Li, Y. Fan, W. Chen, L. Lin, W. Xu, H. Zhuang, Q. Li, Construction of octahedral CoO@CoS composite structure via in-situ synthesis strategy for photocatalytic degradation of tetracycline, Mater. Lett. 315 (January) (2022), 132010, https://doi.org/10.1016/j.matlet.2022.132010.
[20] P.P. Rath, S.S. Bahera, B. Priyadarshini, S.R. Panda, D. Mandal, T. Sahoo, S. Mishra, T.R. Sahoo, P.K. Parhi, Influence of Mg doping on ZnO NPs for enhanced adsorption activity of Congo Red dye, Appl. Surf. Sci. 491 (March) (2019) 256–266, https://doi.org/10.1016/j.apsusc.2019.06.120.
[21] C.M. Taylor, A. Ramirez-Canon, J. Wenk, D. Mattia, Enhancing the photo-corrosion resistance of ZnO nanowire photocatalysts, J. Hazard Mater. 378 (March) (2019), 120799, https://doi.org/10.1016/j.jhazmat.2019.120799.
[22] M.Z.A. Warshagha, M. Muneer, Environmental Nanotechnology , Monitoring & Management Facile synthesis of CdO-ZnO heterojunction photocatalyst for rapid removal of organic contaminants from water using visible light, Environ. Nanotechnol. Monit. Manag. 18 (March) (2022), 100728, https://doi.org/10.1016/j.enmm.2022.100728.
[23] H. Zhang, Y.F. Wang, W.L. Liu, F.G. Kong, M.M. Ren, S.J. Wang, X.Q. Wang, X. L. Duan, D. Peng, Designed synthesis of CoO/CuO/rGO ternary nanocomposites as high-performance anodes for lithium-ion batteries, JOM (J. Occup. Med.) 70 (9) (2018) 1793–1799, https://doi.org/10.1007/s11837-018-2801-8.
[24] E. Suharyadi, A. Muzakki, N.I. Istiqomah, D.L. Puspitarum, B. Purnama, D. Djuhana, Reusability of photocatalytic $CoFe_2O_4$@ZnO core–shell nanoparticles for dye degradation, ECS J. Solid State Sci. Technol. 11 (2) (2022), 023004, https://doi.org/10.1149/2162-8777/ac4c7c.
[25] G. Pérez-Zúñiga, G. Herrera-Pérez, Y. Verde-Gómez, A.M. Valenzuela-Muñiz, Self-assembled ZnO-rGO nanocomposite, a solid-state transformation to control its crystallite size, J. Alloys Compd. 875 (2021), 159992, https://doi.org/10.1016/j.jallcom.2021.159992.
[26] H. Lakhlifi, Y. El Jabbar, S. Guillemet-Fritsch, B. Durand, L. Er-Rakho, R. El Ouatib, Purple nanometrics pigments based on cobalt-doped manganese molybdate: synthesis, characterization, structural, thermal, optical, colorimetric and chemical properties, J. Mol. Struct. 1248 (2022), 131458, https://doi.org/10.1016/j.molstruc.2021.131458.
[27] B. Guo, J. Ma, Y. Shi, K. Zheng, M. Wu, G. Ren, S. Komarneni, Co_3O_4/CoO ceramic catalyst : bisulfite assisted catalytic degradation of methylene blue, Ceram. Int. 47 (19) (2021) 27617–27623, https://doi.org/10.1016/j.ceramint.2021.06.186.
[28] M. Żyła, G. Smoła, A. Knapik, J. Rysz, M. Sitarz, Z. Grzesik, The formation of the Co_3O_4 cobalt oxide within CoO substrate, Corrosion Sci. 112 (2016) 536–541, https://doi.org/10.1016/j.corsci.2016.08.016.
[29] H. Luo, C. Ni, C. Zhang, W. Wang, Y. Yang, W. Xiong, M. Chen, C. Zhou, Y. Zhou, S. Tian, Q. Lin, G. Fang, Z. Zeng, G. Zeng, Lignocellulosic biomass derived N-doped and CoO-loaded carbocatalyst used as highly efficient peroxymonosulfate activator for ciprofloxacin degradation, J. Colloid Interface Sci. 610 (2022) 221–233, https://doi.org/10.1016/j.jcis.2021.11.196.
[30] M. Darbandi, E. Narimani, P.Y. Sefidi, H. Rasouli, M.G. Hosseini, Synthesis of hexagonal cobalt hydroxide and cobalt oxide nanorings as promising materials for oxygen evolution and supercapacitive processes, Int. J. Hydrogen Energy 46 (5) (2021) 3887–3897, https://doi.org/10.1016/j.ijhydene.2020.10.209.
[31] A. Goktas, S. Modanlı, A. Tumbul, A. Kilic, Facile synthesis and characterization of ZnO, ZnO:Co, and ZnO/ZnO:Co nano rod-like homojunction thin films: role of crystallite/grain size and microstrain in photocatalytic performance, J. Alloys Compd. 893 (2022), 162334, https://doi.org/10.1016/j.jallcom.2021.162334.
[32] F. Soleimani, M. Salehi, A. Gholizadeh, Comparison of visible light photocatalytic degradation of different pollutants by (Zn, Mg)$_x$Cu$_{1-x}$Bi$_2$O$_4$ nanoparticles, Ceram. Int. 45 (7) (2019) 8926–8939, https://doi.org/10.1016/j.ceramint.2019.01.224.
[33] A. Pandey, S. Dalal, S. Dutta, A. Dixit, Structural characterization of polycrystalline thin films by X-ray diffraction techniques, J. Mater. Sci. Mater. Electron. 32 (2) (2021) 1341–1368, https://doi.org/10.1007/s10854-020-04998-w.
[34] A. Goktas, S. Modanlı, A. Tumbul, A. Kilic, Facile synthesis and characterization of ZnO, ZnO:Co, and ZnO/ZnO:Co nano rod-like homojunction thin films_ Role of crystallite/grain size and microstrain in photocatalytic performance, J. Alloys Compd. 893 (2022), 162334, https://doi.org/10.1016/j.jallcom.2021.162334.
[35] N. Han, G. Pan, J. Zheng, R. Wang, Y. Wang, Co_{3O4}-ZnO p-n heterostructure nanomaterials film and its enhanced photoelectric response to visible lights at near room temperature, Mater. Res. 22 (3) (2019), https://doi.org/10.1590/1980-5373-MR-2018-0689.
[36] M.W. Kadi, S.I. El-Hout, A. Shawky, R.M. Mohamed, Enhanced mercuric ions reduction over mesoporous S-scheme $LaFeO_3$/ZnO p-n heterojunction photocatalysts, J. Taiwan Inst. Chem. Eng. 138 (August) (2022), 104476, https://doi.org/10.1016/j.jtice.2022.104476.
[37] K.V. Karthik, A.V. Raghu, K.R. Reddy, R. Ravishankar, M. Sangeeta, N.P. Shetti, C. V. Reddy, Green synthesis of Cu-doped ZnO nanoparticles and its application for the photocatalytic degradation of hazardous organic pollutants, Chemosphere 287 (P2) (2022), 132081, https://doi.org/10.1016/j.chemosphere.2021.132081.
[38] A.V. Pashkevich, A.V. Pashkevich, A.K. Fedotov, E.N. Poddenezhny, L.A. Bliznyuk, J.A. Fedotova, N.A. Basov, A.A. Kharchanka, P. Zukowski, T.N. Koltunowicz, O. V. Korolik, V.V. Fedotova, Structure, electric and thermoelectric properties of binary ZnO-based ceramics doped with Fe and Co, J. Alloys Compd. 895 (2022), 162621, https://doi.org/10.1016/j.jallcom.2021.162621.
[39] W.A. Wani, S. Kundu, K. Ramaswamy, H. Venkataraman, Structural, morphological, optical and dielectric investigations in cobalt doped bismuth ferrite nanoceramics prepared using the sol-gel citrate precursor method, J. Alloys Compd. 846 (2020), 156334, https://doi.org/10.1016/j.jallcom.2020.156334.
[40] R. Marsel, N. Imani, T. Kato, D. Oshima, E. Suharyadi, High reusability of green-synthesized Fe_3O_4/TiO_2 photocatalyst nanoparticles for efficient degradation of methylene blue dye, Mater. Today Commun. 33 (September) (2022), 104450, https://doi.org/10.1016/j.mtcomm.2022.104450.
[41] S.M. Mustafa, A.A. Barzinjy, A.H. Hamad, S.M. Hamad, Green synthesis of Ni doped ZnO nanoparticles using dandelion leaf extract and its solar cell applications, Ceram. Int. (2022), https://doi.org/10.1016/j.ceramint.2022.05.202. April.
[42] M. Chandel, V.P. Singh, K. Singha, S. Kalia, R. Kumar, G. Kumar, M. Singh, Structural, magnetic and Mössbauer analysis of lanthanum and nickel doped Co_2Y-type hexaferrite nanomaterial matrix synthesized by sol-gel auto-combustion technique, J. Mol. Struct. 1205 (2020), 127623, https://doi.org/10.1016/j.molstruc.2019.127623.
[43] B. Guo, J. Ma, Y. Shi, H. Zheng, M. Wu, G. Ren, S. Komarneni, Co_3O_4/CoO ceramic catalyst: bisulfite assisted catalytic degradation of methylene blue, Ceram. Int. 47 (19) (2021) 27617–27623, https://doi.org/10.1016/j.ceramint.2021.06.186.
[44] G.M. Al-Senani, N.M. Deraz, O.H. Abd-Elkader, Magnetic and characterization studies of CoO/Co3O4 nanocomposite, Processes 8 (7) (2020) 844, https://doi.org/10.3390/pr8070844.
[45] M. Achehboune, M. Khenfouch, I. Boukhoubza, L. Leontie, C. Doroftei, A. Carlescu, G. Bulai, B. Mothudi, I. Zorkani, A. Jorio, Microstructural, FTIR and Raman spectroscopic study of Rare earth doped ZnO nanostructures, Mater. Today Proc. 53 (2021) 319–323, https://doi.org/10.1016/j.matpr.2021.04.144.
[46] N. Alam, K. Tahir, S. Nazir, A.U. Khan, K. Albalawi, M.S. Refat, Z.M. Almarhoon, V. Jevtovic, H.S. Al-Shehri, A.M. Aldawsari, Effect of light-dark conditions on inhibition of Gram positive and gram negative bacteria and dye decomposition in the presence of photocatalyst Co/ZnO nanocomposite synthesized by ammonia evaporation method, Photodiagnosis Photodyn. Ther. 38 (January) (2022), 102853, https://doi.org/10.1016/j.pdpdt.2022.102853.
[47] F.H. Abdullah, N.H.H. Abu Bakar, M. Abu Bakar, Low temperature biosynthesis of crystalline zinc oxide nanoparticles from Musa acuminata peel extract for visible-light degradation of methylene blue, Optik 206 (January) (2020), 164279, https://doi.org/10.1016/j.ijleo.2020.164279.
[48] M. Abdelkrim, M. Guezzoul, M. Bedrouni, M. Bouslama, A. Ouerdane, B. Kharroubi, Effect of slight cobalt incorporation on the chemical, structural, morphological, optoelectronic, and photocatalytic properties of ZnO thin film,

J. Alloys Compd. 920 (2022), 165703, https://doi.org/10.1016/j.jallcom.2022.165703.
[49] P.R. Jubu, O.S. Obaseki, A. Nathan-abutu, F.K. Yam, Y. Yusof, M.B. Ochang, Results in Optics Dispensability of the conventional Tauc ' s plot for accurate bandgap determination from UV – vis optical diffuse reflectance data, Results Opt. 9 (July) (2022), 100273, https://doi.org/10.1016/j.rio.2022.100273.
[50] T. Sansenya, N. Masri, T. Chankhanittha, T. Senasu, J. Piriyanon, S. Mukdasai, S. Nanan, Hydrothermal synthesis of ZnO photocatalyst for detoxification of anionic azo dyes and antibiotic, J. Phys. Chem. Solid. 160 (August 2021) (2022), 110353, https://doi.org/10.1016/j.jpcs.2021.110353.
[51] W. Shi, F. Guo, C. Zhu, H. Wang, H. Li, H. Huang, Y. Liu, Z. Kang, Carbon dots anchored on octahedral CoO as a stable visible-light-responsive composite photocatalyst for overall water splitting, J. Mater. Chem. 5 (37) (2017) 19800–19807, https://doi.org/10.1039/c7ta06077g.
[52] J. Lu, H. Alib, J. Hurhb, Y. Hana, I. Batjikhb, E.J. Rupaa, G. Anandapadmanaban, J. K. Park, D.C. Yang, The assessment of photocatalytic activity of zinc oxide nanoparticles from the roots of Codonopsis lanceolata synthesized by one-pot green synthesis method, Optik 184 (March) (2019) 82–89, https://doi.org/10.1016/j.ijleo.2019.03.050.
[53] S. Siva Kumar, V. Ranga Rao, G. Nageswara Rao, Effect of morphology, crystallite size and optical band gap on photocatalytic activity of ZnO nanostructures for decolorization of R6G, Mater. Today Proc. 62 (2022) 5494–5502, https://doi.org/10.1016/j.matpr.2022.04.220.
[54] M. Xu, M. Sun, S. ur Rehman, K. Ge, X. Hu, H. Dinga, J. Liub, H. Bi, One-pot synthesis of CoO–ZnO/rGO supported on Ni foam for high-performance hybrid supercapacitor with greatly enhanced cycling stability, Chin. Chem. Lett. 32 (6) (2021) 2027–2032, https://doi.org/10.1016/j.cclet.2020.12.011.
[55] S. Barman, A.K. Kundu, K.S.R. Menon, Journal of Magnetism and Magnetic Materials influence of finite Size and Image Charge Screening on the Antiferromagnetic Ordering of CoO ultrathin films, vol. 515, 2020, https://doi.org/10.1016/j.jmmm.2020.167292. August.
[56] Q. Dai, J. Tang, The optical and magnetic properties of CoO and Co nanocrystals prepared by a facile technique, Nanoscale 5 (16) (2013) 7512–7519, https://doi.org/10.1039/c3nr01971c.
[57] R.V. Santos, G.A.C. Pasca, C.S. Costa, B.B. Santo, L. Otubo, L.F.D. Pereira, B. S. Correa, F.B. Effenberger, A. Burimova, R.S. Freita, A.W. Carbonari, Crystalline and magnetic properties of CoO nanoparticles locally investigated by using radioactive indium tracer, Sci. Rep. 11 (1) (2021) 1–13, https://doi.org/10.1038/s41598-021-99810-y.
[58] R. Li, F. Zhang, Y. Hu, Performance of switch between exchange bias and coercivity: influences of antiferromagnetic anisotropy and exchange coupling, J. Mater. Sci. Technol. 120 (2022) 186–195, https://doi.org/10.1016/j.jmst.2021.12.053.
[59] J. Sin, S. Lam, H. Zeng, H. Lin, H. Li, Enhanced synchronous photocatalytic 4-chlorophenol degradation and Cr(VI) reduction by novel magnetic separable visible-light-driven Z-scheme $CoFe_2O_4$/P-doped BiOBr heterojunction nanocomposites, Environ. Res. 212 (PC) (2022), 113394, https://doi.org/10.1016/j.envres.2022.113394.
[60] Y.H. Chin, J.C. Sin, S.M. Lam, H. Zeng, H. Lin, H. Li, amd A.R. Mohamed, 0-D/3-D heterojunction composite constructed by decorating transition metal oxide nanoparticle on peony-like ZnO hierarchical microstructure for improved photodegradation of palm oil mill effluent, Optik 260 (February) (2022), 169098, https://doi.org/10.1016/j.ijleo.2022.169098.
[61] G. Rytwo, A.L. Zelkind, Evaluation of kinetic pseudo-order in the photocatalytic degradation of ofloxacin, Catalysts 12 (1) (2022) 1–11, https://doi.org/10.3390/catal12010024.
[62] A. Mohammadzadeh, M.K. Pireyousefan, B.S. Ravasjan, M. Azadbeh, H. Rashedi, M. Dibazar, A. Mostafaei, Synergetic photocatalytic effect of high purity ZnO pod shaped nanostructures with H_2O_2 on methylene blue dye degradation, J. Alloys Compd. 845 (2020), 156333, https://doi.org/10.1016/j.jallcom.2020.156333.
[63] X. Zhang, N. Yuan, T. Chen, B. Li, Q. Wang, Fabrication of hydrangea-shaped Bi2WO6/ZIF-8 visible-light responsive photocatalysts for degradation of methylene blue, Chemosphere 307 (P4) (2022), 135949, https://doi.org/10.1016/j.chemosphere.2022.135949.
[64] A. Hamrouni, H. Azzouzi, A. Rayes, L. Palmisano, R. Ceccato, F. Parrino, Enhanced solar light photocatalytic activity of ag doped tio2-ag3po4 composites, Nanomaterials 10 (4) (2020) 1–16, https://doi.org/10.3390/nano10040795.
[65] S.M. Lam, M.K. Choong, J.C. Sin, H. Zeng, L. Huang, L. Hua, H. Li, Z.H. Jaffari, K. H. Cho, Construction of delaminated Ti_3C_2MXene/$NiFe_2O_4$/V_2O_5 ternary composites for expeditious pollutant degradation and bactericidal property, J. Environ. Chem. Eng. 10 (5) (2022), 108284, https://doi.org/10.1016/j.jece.2022.108284.
[66] J. Kelly, C. McDonnell, N. Skillen, P. Manesiotis, P.K.J. Robertson, Enhanced photocatalytic degradation of 2-methyl-4-chlorophenoxyacetic acid (MCPA) by the addition of H_2O_2, Chemosphere 275 (2021), 130082, https://doi.org/10.1016/j.chemosphere.2021.130082.
[67] M. Adeel, M. Saeed, I. Khan, M. Muneer, N. Akram, Synthesis and Characterization of Co−ZnO and Evaluation of its Photocatalytic Activity for Photodegradation of Methyl Orange, vol. 6, 2021, pp. 1426–1435, https://doi.org/10.1021/acsomega.0c05092.
[68] H.Y. Al-Gubury, Q.Y. Mohammed, Prepared coupled ZnO-Co_2O_3 then study the photocatalytic activities using crystal violet dye, J. Chem. Pharmaceut. Sci. 9 (3) (2016) 1161–1165.